Post Referee Draft

Conditions for Nucleation and Growth in the Substrate Boundary Layer at

Plasma Spray-Physical Vapor Deposition (PS-PVD)

Georg Mauer<sup>1</sup>, Robert Vaßen

Forschungszentrum Jülich GmbH, Institut für Energie- und Klimaforschung (IEK-1)

Jülich, Germany

Abstract

Plasma spray-physical vapor deposition (PS-PVD) is a novel coating process based on plasma spraying. In

contrast to conventional methods, deposition can come off not only from liquid splats but also from

vapor phase. Moreover, there is the suggestion that also nano-sized clusters can be formed by

homogeneous nucleation and contribute to deposition. In this work, the conditions for nucleation and

growth of such nano-sized particles in the plasma flow around the substrate under PS-PVD conditions

were investigated. A boundary layer kinetics model was coupled to an approach for homogeneous

nucleation from supersaturated vapors and primary particle growth by condensation as well as

secondary particle formation by coagulation. The results confirm the importance of the boundary layer

on the substrate. However, since these particles are relatively small, their contribution to coating

deposition is limited. Furthermore, microstructure or crystallographic orientations are unlikely to be

affected by this cluster deposition.

<sup>1</sup> Corresponding author

Dr. Georg Mauer

Forschungszentrum Jülich GmbH, Institut für Energie- und Klimaforschung (IEK-1)

52425 Jülich, Germany

# **Keywords**

- Plasma Spray-physical vapor deposition
- Evaporation
- Nucleation
- Condensation
- Cluster

### 1 Introduction

Plasma Spray-Physical Vapor Deposition (PS-PVD) was developed on the basis of conventional low-pressure plasma spraying processes (LPPS, formerly often termed vacuum plasma spraying, VPS) operating at 5-20 kPa. By lowering the chamber pressure to 50-200 Pa and considerable enhancement of the plasma power up to 180 kW, PS-PVD enables to evaporate the feedstock material to a substantial amount so that deposition takes place also from the vapor phase [1, 2]. This allows to obtain advanced microstructures and also non-line-of-sight deposition, as applied e.g. for columnar structured thermal barrier coatings (TBCs) [3, 4, 5, 6, 7]. As PS-PVD is a quite novel process it is still under research. To the best knowledge of the authors, scientists in China, Germany, Switzerland, Poland, and in the US are currently working in this field; however, industrial applications are still not disclosed.

The deposition mechanisms of PS-PVD coatings are not yet fully understood. In [8], it is shown that substrate temperature and deposition rate considerably influence the coating microstructures; a corresponding preliminary structure zone model was proposed. Similar findings were reported by Li et al. [9] It is an open question whether there is also a transition in the nature of the deposits from molecules to nano-sized clusters (termed also as particles in this work) which could influence the formation of the microstructure. Furthermore, crystallographic textures were identified in case of relatively high substrate temperatures and low deposition rates [8]. It is assumed that under such conditions mainly molecules are deposited, which are still mobile by surface diffusion after being adsorbed on the substrate surface. Thus,

the question on the nature of the deposits is suggested again, however, at different dimensional scales as compared to microstructure formation.

The formation of nano-sized particles by gas-phase nucleation from supersaturated conditions in thermal plasmas was utilized specifically to deposit nano-structured coatings at high growth rates [10, 11] and for powder synthesis [12, 13, 14]. In the context of coating technologies, several researchers emphasized the importance of the boundary layer for the formation and deposition of nano-sized particles, see e.g. the reviews on thermal plasma processing methods of Yoshida [15, 16, 17] and Shigeta and Murphy [18] as well as in the work of other researchers at the University of Tokyo [19, 20]. In [21], Han and Yoshida describe the deposition of Si by quenching Si vapor in the boundary layer above the substrate yielding supersaturated conditions followed by the generation and coagulation of Si clusters. They found that clusters in the range < 1 nm were the dominant component among the deposited species [22]. Terashima et al. reported that such clusters have a higher sticking probability than atoms, especially at high temperatures; moreover they can be rearranged after impaction onto the substrate [19]. Bouyer et al. [23] found that the growth of Si<sub>3</sub>N<sub>4</sub> fibers proceeds from nanoparticles which nucleate in the boundary layer above the fiber tips. They discussed the required conditions and concluded that the formation is favored by low substrate temperatures and small boundary layer thickness limiting particle growth by condensation and coagulation.

In this work, it was studied whether the flow conditions in the boundary layer close to the substrate could influence the nature of PS-PVD deposits. In particular, the possibility of homogeneous nucleation and particle growth in the plasma gas flow was investigated and what is the significance of cluster vs. direct vapor deposition by heterogeneous nucleation on the substrate can be. Developing the calculation models for this, valuable suggestions were received from the analysis of fume formation mechanisms in

arc welding by Tashiro, Murphy, et al. They coupled nucleation, condensation, and coagulation approaches with process models for gas metal arc and gas tungsten arc welding [24, 25].

### 2 Process Conditions and Material Data

The PS-PVD experiments were carried out on a Multicoat System (Oerlikon Metco, formerly Sulzer Metco, Wohlen, Switzerland). The feedstock powder was zirconia partially stabilized by 7 wt% yttria (YSZ); it was injected into a plasma gas mixture of 35 slpm Ar and 60 slpm He (slpm standard liters per minute). The mole fraction of ZrO<sub>2</sub> was 0.013 corresponding to a powder feed rate of 7 g / min. For additional calculations, also a powder feed rate of 20 g / min was considered corresponding to a ZrO<sub>2</sub> mole fraction of 0.037. Complete evaporation is assumed which is possible under ideal powder injection conditions as shown by the calculations reported in [2]. The gas mixture was expanded through the nozzle of the single cathode O3CP plasma torch (Oerlikon Metco) into the process chamber where the pressure was kept at 200 Pa by means of large vacuum pumps. This plasma jet is under-expanded and exits the nozzle at supersonic conditions. **Table 1** gives the plasma gas characteristics at the two investigated spray distances of 400 mm and 1000 mm. The indicated plasma gas velocities are based on estimations in [26], the temperatures result from OES measurements [27]. Graphite was used as a substrate material. The given substrate surface temperatures were measured pyrometrically. A temperature drop was observed at the sample edges estimated as approx. 20% at a radial offset of 50 mm.

Since for YSZ physical data at high temperatures are available only to a limited extend, material data for pure zirconia were used in this work. The mass of a  $ZrO_2$  molecule is  $m_I = M/N_A = 2.05 \cdot 10^{-25}$  kg where M = 123.2188 kg kmol<sup>-1</sup> is the molar mass and  $N_A = 6.022 \cdot 10^{23}$  is the Avogadro number. With the density

of zirconia  $\rho_p$  = 6.27 kg m<sup>-3</sup>, the volume of a molecule  $v_I$  = 3.26  $10^{-29}$  m<sup>3</sup> can be calculated. Assuming a spherical shape, the surface area  $s_I$  = 4.94  $10^{-19}$  m<sup>2</sup> was obtained from this. The surface tension of liquid zirconia was estimated to be  $\sigma$  = 1.2 N m<sup>-1</sup> based on [28]. A more precise determination for materials with high melting points like ZrO<sub>2</sub> is hardly possible [29]. The temperature-dependent dynamic viscosity  $\mu$  /(Pa s) = 0.0037 exp(6110 K / T) was taken from [30].

The chemical equilibrium of ZrO<sub>2</sub>, ZrO, Zr, O<sub>2</sub>, and O in the Ar-He plasma gas mixture was calculated for PS-PVD conditions using the CEA2 code [31, 32]. Here, the chemical equilibrium conditions are determined by the minimization of the Gibbs energy. This is performed by an iterative procedure. The results in Fig. 1 show that, above approx. 4800 K, only Zr and O are present. Below, gaseous ZrO is formed before ZrO<sub>2</sub> appears beneath 3800 K. Ionized gaseous species are minor fractions of ZrO<sup>+</sup> above 2700 K and Zr<sup>+</sup> above 3250 K. Only very small amounts of molecular oxygen O<sub>2</sub> are found between 2660 K and 3600 K (not plotted). At 2720 K, solid cubic zirconia is generated which transforms to the tetragonal phase at 2630K. In Fig. 1, just the sum of these two solid phases is given. As long as solid zirconia is present, gaseous zirconia vapor is formed; beyond it dissociates which leads to the abrupt variations. In contrast to higher pressures, there is no liquid ZrO<sub>2</sub> phase present at 200 Pa. Solid zirconia formation takes place mainly from ZrO<sub>2</sub> vapor rather than from ZrO reacting with O. For this reason, only homogeneous nucleation and condensation of ZrO<sub>2</sub> is considered in this work. It must be noted that all these calculation results are valid for equilibrium conditions and that under PS-PVD conditions there might be deviations due to the short time scales.

**Fig. 2** shows total vapor pressure data of ZrO<sub>2</sub> according to a calculated fit [7] of literature data obtained from [33, 34],

$$\log \left( \frac{p_{vap,tot}}{P_a} \right) = 13.8778 - \frac{36046 \text{ K}}{T}$$
 (Equ. 1)

Moreover, the total partial pressure of all gaseous species generated by the evaporation of zirconia was calculated from the equilibrium molar fractions using the CEA2 code and superimposed to the fit of the total ZrO<sub>2</sub> vapor pressure. Both curves are in good agreement in the saturated range. It is obvious, that the partial pressure corresponds to the total vapor pressure at approximately 2720 K, as already mentioned above. Below this temperature and under equilibrium conditions, condensation takes place and the partial pressure curve decreases congruently with the vapor pressure curve. Diverging from this, the dotted curve indicates the development of supersaturation during fast cooling schematically. Only when a specific supersaturation ratio is reached, the zirconia vapor partial pressure turns down since nucleation and growth are initiated and consume gaseous zirconia species.

# 3 Calculation Principles and Assumptions for Nucleation and Growth

The formation of nano-sized clusters from the feedstock's vapor phase is determined by the following mechanisms,

- <u>Supersaturation</u> of the plasma gas mixture containing the vaporized feedstock species by cooling;
- Formation of <u>primary particles</u> with critical size (minimum size at which the nuclei are stable and do not decay) from supersaturated vapor;
- Growth of primary particles by physical condensation [35];
- Formation of <u>secondary particles</u> by <u>coagulation</u>, i.e. either by <u>coalescence</u> (merging of liquid or solid particles forming a new shape) or by <u>agglomeration</u> (clustering of particles retaining their shapes), each generally influenced by laminar shear, turbulence, convection, charging, thermophoresis, Brownian motion, etc.

These mechanisms are modelled following a single stream line using a monodisperse approach.

### 3.1 Homogeneous Nucleation Model

In the PS-PVD process, particle nucleation is assumed to be driven by physical condensation of supersaturated vapor rather than chemical reactions [36]. Moreover, it is unlikely that this nucleation is ion-induced since the ionization degrees in the plasma jet at PS-PVD conditions were found to be small [27]. Thus, only electrically neutral particles are considered and charge effects are neglected.

The fast cooling and thus the rapid increase of the supersaturation ratio as found in PS-PVD at the periphery of the plasma jet and the flow around the substrate to be coated is assumed to favor the mechanisms of homogeneous nucleation [13]. The calculation results given in section 2 have already shown that the formation of solid zirconia under PS-PVD conditions takes place mainly from ZrO<sub>2</sub> vapor. Thus, the gas phase reaction rates to form condensable ZrO<sub>2</sub> molecules are expected to be significant higher than those of Zr, ZrO, and O at the particle surface or within the condensed phase. Accordingly, the nucleation rate is calculated on the basis of the homogeneous nucleation theory.

Assuming spherical particles, their critical size results from the Kelvin equation [37]

$$d_p^* = \frac{4 \sigma v_1}{k_B T \ln S}$$
 (Equ. 2)

where  $k_B$  is the Boltzmann constant (1.38  $10^{-23}$  J K<sup>-1</sup>), T the gas temperature (K), and  $S = n_1/n_s$  is the supersaturation ratio (dimensionless) with  $n_1$  the vapor molecule concentration (m<sup>-3</sup>), and  $n_s$  the vapor molecule concentration at saturated state (m<sup>-3</sup>). Homogeneous nucleation occurs only if S > 1.

Introducing the normalized surface tension  $\theta$  =  $\sigma$   $s_1/k_B$  T (dimensionless), the number of molecules in a critical nucleus is

$$g^* = \left(\frac{2 \theta}{3 \ln S}\right)^3 \tag{Equ. 3}$$

This is part of the classical theory of homogeneous nucleation as reported by [38]. It was extended by [39] to obtain the "kinetic" nucleation rate expression by

$$J = \frac{\beta_{1,1} n_s^2 S}{12} \sqrt{\frac{\theta}{2\pi}} \exp\left[\theta - \frac{4\theta^3}{27(\ln S)^2}\right]$$
 (Equ. 4)

where J is the number of nuclei generated per unit time and volume (s<sup>-1</sup>m<sup>-3</sup>) and  $\beta_{1,1}$  the collision function between two vapor molecules (m<sup>3</sup>s<sup>-1</sup>).

Particles smaller than about 1  $\mu$ m collide and merge as a result of their Brownian motion [40]. If the particles are significantly smaller than the mean free path of the gas, free molecular flow prevails. The particle Knudsen number is  $\mathrm{Kn_p}=\lambda/d_p$  where  $\lambda$  is the mean free path (m) and  $d_p$  the particle diameter (m). Presuming free molecular flow which is typically indicated by  $(\mathrm{Kn_p}>10)$  for the small particles in the plasma jet at PS-PVD conditions [2], the collision function  $(\mathrm{m^3s^{-1}})$  is derived according to [41] from the kinetic gas theory. For spherical particles containing i and j molecules (i-mers and j-mers), respectively, it is given by

$$\beta_{i,j} = \left(\frac{3v_1}{4\pi}\right)^{1/6} \sqrt{\frac{6k_B T}{\rho_p} \left(\frac{1}{i} + \frac{1}{j}\right)} \left(i^{1/3} + j^{1/3}\right)^2$$
 (Equ. 5)

The collision function for two vapor molecules (monomers) in Equ. 5 simplifies to

$$\beta_{1,1} = 4 \left(\frac{3v_1}{4\pi}\right)^{1/6} \sqrt{\frac{12 k_B T}{\rho_p}}$$
 (Equ. 6)

The steady-state features of cluster formation will only be reached when transient effects have disappeared from the system [42]. The time constant  $\tau^*$  for the approach of the nucleation rate to steady-state  $J_{g^*}(t) = J\left(1-\exp(-t/\tau^*)\right)$  can be estimated according to [43] by

$$au^* = rac{1}{2C_{i*}Z_{i*}^2}$$
 (Equ. 7)

where  $Z_{i*} = (\gamma/(2\pi k_B T))^{\gamma_2}$  is the Zeldovich factor with  $\gamma = 8\pi s_1 \sigma/(9 g^{*\gamma_2})$ , and  $C_{i*} = 4\pi s_1 g^{*\gamma_2} n_1 (k_B T/(2\pi m_1))^{\gamma_2}$  is the condensation coefficient.

Applying the mentioned approach for homogeneous nucleation in the current work, some important restraints must be noted:

- An important limitation is the use of the bulk surface tension as it might be not applicable to very small clusters [40]. However, no more sophisticated data is available for such high melting materials like zirconia.
- The Kelvin relationship (Equ. 2) holds best for particles with g > 10 molecules. However, at highly saturated conditions, the critical nuclei sizes can approach molecular dimensions. Nevertheless, it is also applied for an order of magnitude estimate down to molecular dimensions [40]. Alternatively, some researchers treat all gas molecules as stable nuclei if g \* < 2 [44] and equate the nucleation rate with  $J = \frac{1}{2} \beta_{11} \, n_1^2$  assuming that all molecular collisions are effective. In the present work, this was not followed as this led to discontinuities in the development of the nucleation rate. And anyway, these values did not differ considerably from those obtained from Equ. 4.

- Another assumption is that a quasi-steady state of nucleation exists [40]. If the time scales of
  velocity and temperature changes in the boundary layer are significantly larger than the time
  constants for nucleation, the used approach is applicable.
- In principle, the zirconia particles nucleate as liquid droplets or directly to the solid phase.

  Although the nucleation model used in this work is restricted to the formation of liquid droplets,
  i.e. structureless spheres, it can be argued that the qualitative trends regarding the effects of concentrations and cooling rates should be valid also for nucleation directly to the solid [35].

# 3.2 Condensation Model of Nucleated Particles

For the free molecular flow regime, the collision function for single molecules and particles containing g molecules can be obtained using Equ. 5 and setting i=1 and j=g.

$$\beta_{1,g} = \left(\frac{3v_1}{4\pi}\right)^{1/6} \sqrt{\frac{6k_B T}{\rho_p} \left(1 + \frac{1}{g}\right)} \left(1 + g^{1/3}\right)^2$$
 (Equ. 8)

Condensation is possible only if S > 1. In this case it is assumed that each collision of a monomer and a particle leads to condensation. On the other hand, re-evaporation of condensed molecules must be also considered (see below section 3.4).

# 3.3 Coagulation Model of Nucleated Particles

In the free molecular flow regime, the collision function for particles containing g molecules can be obtained using Equ. 5 and setting i=j=g yielding

$$\beta_{g,g} = \left(\frac{3v_1}{4\pi}\right)^{1/6} \sqrt{\frac{6k_B T}{\rho_p}} \frac{2}{g} \left(2 g^{1/3}\right)^2$$
 (Equ. 9)

Coagulation is not limited to S > 1. It is assumed that each collision of two particles leads to coagulation. A factor of  $\frac{1}{2}$  is introduced in order to avoid double counting of particle-particle collisions (see section 3.4).

The particle shape resulting from coagulation depends on how much time is available to form a spherical particle before the next collision with another particle occurs. In case of <u>liquid</u> initial particles, the time required for merging to a secondary spherical particle (coalescence) is given by Frenkel [45]

$$au_{coal,liqu} = \frac{\mu \, d_{p,f}}{\sigma}$$
 (Equ. 10)

where  $d_{p,f}$  is the final spherical particle diameter after coalescence is completed which results from the volumes of the two initial particles. Data for the dynamic viscosity  $\mu$  and the surface tension  $\sigma$  of zirconia are given in section 2.

If the colliding particles are <u>solid</u>, the formation of a spherical secondary particle is possible provided that there is sufficient time for coalescence by solid-state diffusion. The corresponding characteristic time is given by Friedlander et al. [46]

$$\tau_{coal,sol} = \frac{3 k_B T g}{64 \pi \sigma D}$$
 (Equ. 11)

where *D* is the diffusion coefficient expressed by

$$D = D_0 \exp\left(\frac{-Q}{RT}\right)$$
 (Equ. 12)

The diffusivity  $D_0$  is set to  $D_0 = 1 \cdot 10^{-3} \,\mathrm{m^2 \, s^{-1}}$  and the activation energy to  $Q = 314 \,\mathrm{kJ \, mol^{-1}}$  for surface diffusion of zirconia according to Cipitria [47]; R is the universal gas constant  $R = 8.3145 \,\mathrm{J \, mol^{-1} \, K^{-1}}$ .

The characteristic time-scale of particle collision  $au_{coll}$  is expressed by

$$au_{coll} = rac{2}{eta_{gg} n_g}$$
 (Equ. 13)

where the collision function  $\beta_{gg}$  is calculated by Equ. 9 and  $n_g$  is the particle density per unit gas volume (see below section 3.4). If particles, either in liquid or solid state, coalesce faster than they collide (i.e.  $\tau_{coal} << \tau_{coll}$  [48]) spherical secondary particles are obtained. Otherwise, aggregation of the initial particles is assumed to yield irregularly shaped agglomerates.

# 3.4 Description of nucleation and growth evolution in time

A system of simple ordinary differential equations is used to describe the evolution in time of nucleation, condensation/evaporation, and coagulation to determine the molecule density in the gas phase, the concentration of particles, and their average size [49]. The approach is based on a monodisperse approximation and thus simple and effective in contrast to more complex and elaborate methods using the moments of a size distribution function. It was reported to deliver results in good agreement with those obtained by more elaborate discrete-type or moment-type methods [49].

The approach distinguishes between single molecules (monomers, indicated by subscript 1) and particles containing an average number g of monomers (g-mers, indicated by subscript g). The first differential equation can be formed based on the fact that nucleation contributes to the particle number concentration, while coagulation reduces it

$$\frac{d}{dt}n_g = J - \frac{1}{2}\beta_{g,g} n_g^2$$
 (Equ. 14)

where t is the time (s) and  $n_g$  is the number concentration of g-mer particles per unit volume (m<sup>-3</sup>). The coagulation term is a particular application of the Smoluchowski population balance equation [50] for the monodisperse approach.

Moreover it can be stated that the total volume of the particles changes because new particles are generated by nucleation and by particle growth due to condensation, while it is not affected by coagulation

$$\frac{d}{dt}(n_g v_g) = J v_1 g^* + v_1 \beta_{1,g}(n_1 - n_s) n_g$$
 (Equ. 15)

where  $v_g$  is the average particle volume. The introduction of the term  $-n_s$  takes account for reevaporation.

The third condition is that the total amount of matter does not change in time; i.e., the total volume of monomers  $n_1v_1$  (still not nucleated) plus the total volume of particles  $n_gv_g$  is constant

$$\frac{d}{dt}(n_1 \ v_1 + n_g \ v_g) = 0 \tag{Equ. 16}$$

This equation can be rearranged giving the change rate of the monomer density in time

$$\frac{d}{dt}n_1 = -\frac{1}{v_1}\frac{d}{dt}(n_g v_g) \tag{Equ. 17}$$

which can be combined with Equ. 15.

Thus, the evolution in time of the monomer number density  $n_I$ , the particle number density  $n_g$ , and the average particle volume  $v_g$  can be determined on the basis of the system of equations containing Equ.

17, Equ. 14, and Equ. 15. The equations were numerically calculated using an integration scheme with constant time intervals and appropriate starting conditions. In order to review the convergence performance of this approach, several calculations were performed for evaporation of zirconia in an argon helium mixture at 200 Pa and 2000 K. Different time steps for numerical integration were used between  $10^{-5}$  and  $10^{-7}$  s. The final monomer number density  $n_I$ , the particle number density  $n_g$ , and the average particle diameter  $< d_p >$  obtained at  $t = 10^{-4}$  s were plotted against the time width for numerical integration  $\Delta t$  applied in each case, **Fig. 3**. By refining the time steps down to  $1 \cdot 10^{-7}$  s, no significant improvements of the results are achieved anymore since the results converge very close against steady-state values. To be on the safe side, time increments between  $9.6 \cdot 10^{-8}$  s and  $4.9 \cdot 10^{-7}$  s were applied for the numerical calculations in this work. They do not reflect the time scales of nucleation.

#### 4 PS-PVD flow model

In order to determine the temperature development along a stream line to follow the quenching of the plasma/vapor mixture, two locations are of interest, where the temperatures become sufficiently low so that adequate supersaturation for nucleation and growth is reached. This is on the one hand the edge of the plasma jet where cooling takes place by convection and cold surrounding gas may be entrained. On the other hand, this is the flow in the boundary layer around the comparatively cold substrate. The latter case is the focus of this work.

## 4.1 Boundary Layer

The motion of the fluid molecules in the boundary layer is described applying a particular solution of the Navier-Stokes equations for viscous flows. In contrast, free molecular flow would prevail if the mean free path of the fluid molecules became distinctly larger than the diameter of the flow. This is typically found

in the high and ultrahigh vacuum regime at pressures considerably below 0.1 Pa and mean free path lengths above 100 mm. However, at PS-PVD conditions, viscous fluid-like behavior can be assumed as the scale of the flow is large with respect to the magnitudes of the mean free path. Besides, this approach yields steady velocity fields so that streamlines can be calculated without difficulty by numerical integration as described at the end of this section.

The flow model considers an axisymmetric flow normal to a plate (substrate) which is shown schematically in **Fig. 4**. The potential flow which is frictionless (non-viscous) far from the substrate is

$$v_{r,\infty} = a r, \ v_{\omega,\infty} = 0, \ v_{z,\infty} = -2 a z$$
 (Equ. 18)

where v is the flow velocity in the cylindrical coordinate directions r,  $\phi$ , and z;  $\infty$  denotes a location far from the surface and a is the strength of the flow (s<sup>-1</sup>). In the boundary layer  $\delta$  however, the viscosity must be considered to fulfill the non-slip condition at the substrate surface. If v is the kinematic viscosity of the fluid (m<sup>2</sup> s<sup>-1</sup>) the similarity transformation

$$v_r = v_{r,\infty} f'(\eta) = a r f'(\eta), \ v_{\varphi} = 0, \ v_z = -2 \sqrt{v a} f(\eta), \ \eta = z \sqrt{a/v}$$
 (Equ. 19)

reduces the Navier-Stokes equation to

$$f''' + 2 f f'' - (f')^2 + 1 = 0$$
 (Equ. 20)

This differential equation was initially solved by [51] applying the boundary conditions f(0) = 0, f'(0) = 0, and  $f'(\infty) = 1$ . Using the tabulated solutions of Equ. 20 calculated by [52], the thickness of the boundary layer can be determined. The surface distance where the tangential flow velocity  $v_r$  reaches 99% of its final value  $v_{r,\infty}$  is defined as boundary layer thickness  $\delta_v$ . For the axisymmetric flow, this condition  $v_r = 0.99 \ v_{r,\infty} \rightarrow f'(\eta) = 0.99$  (cf. Equ. 19) is fulfilled for approx.  $\eta = 2.8$  [52] so that the boundary layer thickness is

$$\delta_v = 2.8 \sqrt{\frac{v}{a}}$$
 (Equ. 21)

**Table 2** gives the boundary layer data at the two investigated spray distances. The kinematic viscosities were calculated by means of CEA2 for the mean boundary layer temperature in each case determined by integration along the boundary layer thickness. The flow strengths were found iteratively to achieve the corresponding plasma velocities of  $v_{z,\infty}$  = -1400 m s<sup>-1</sup> and  $v_{z,\infty}$  = -1200 m s<sup>-1</sup>, respectively, at the top of the boundary layer, cf. estimation in section 2, **Table 1**. Then, the boundary layer thicknesses could be determined applying Equ. 21. As the boundary layer thickness is dependent not only from the kinematic viscosity but also from the flow field strength, both effects are counterbalanced so that the same thicknesses were obtained.

Analogous to the velocity boundary layer, there is a temperature boundary layer adjacent to the substrate surface due to convective heat transfer. In order to determine its thickness  $\delta_T$ , an appropriate approach for gases is  $\delta_T/\delta_v \approx \Pr^{-1/3}$  [53]. For the present conditions, the Prandtl number (calculated by CEA2 for average boundary layer temperatures) is  $\Pr = 0.65$  at 400 mm distance and  $\Pr = 0.68$  at 1000 mm. Thus,  $\Pr^{-1/3}$  is not far from unity so that in this work the same boundary layer thicknesses for friction and convection were applied. The shape of the temperature profile between the top of the boundary layer and the substrate surface was assumed to be parabolic with the boundary conditions  $T(z=0) = T_{sub}$ ,  $T(z=\delta) = T_{\infty}$  (cf. measured temperatures in section 2, Table 1), and  $dT/dz(z=\delta) = 0$ . Furthermore, the observed temperature drop of 20% was considered at a radial offset of 50 mm.

The modelling domain of the boundary layer was between r=0 mm (plasma jet axis) and r=60 mm. Three flow filaments through the boundary layer were modelled originating on the top of the boundary layer at different radial distances to the jet center. The local velocities  $v_r$  and  $v_z$  and the transformed coordinate  $\eta$  were calculated by Equ. 19. For this,  $f(\eta)$  and  $f'(\eta)$  were taken from tabulated data given in [51] and interpolated by a fourth order polynomial fit (coefficient of determination  $r^2 > 0.9999$ ). The kinematic viscosity of the plasma gas v was calculated for several temperatures between the plasma and the substrate temperature by CEA2 and fitted by an exponential function ( $r^2 = 0.9996$ ). Finally, the stream line points (r, z) were obtained from the local velocities using the same numerical integration scheme and time steps as applied for nucleation and condensation (cf. section 3.4). From this, the temperature development in time is known along each stream line. Finally, the corresponding local vapor pressures of zirconia can be determined by Equ. 1.

## 4.2 Thermophoresis

Due to the high temperature gradient occurring in the boundary layer, thermophoretic forces could have an impact on the particle movement as they are driven from high to low temperature regions. For large particle Knudsen numbers (i.e.  $d_p \ll \lambda$ ), the thermophoretic velocity is independent on the particle size and can be calculated by [40]

$$\vec{v}_T = \frac{-3 \nu \nabla T}{4 (1 + \pi^{\alpha}/8) T}$$
 (Equ. 22)

where  $\alpha$  is the thermal accommodation coefficient; according to Chen [54]  $\alpha$  = 0.8 can be set. The r and z components of the local temperature gradient  $\nabla T$  can easily be calculated deriving the parabolic temperature distribution approach for the boundary layer (cf. section 4.1).

# 4.3 Diffusion

According to [55], the average quadratic displacement per unit time by diffusion is

$$\frac{\bar{x}^2}{\Delta t} = \frac{2k_B T}{f}$$
 (Equ. 23)

where f is the friction coefficient. For free molecular flows it can be expressed by [40]

$$f = \frac{2}{3} d_p^2 \rho_{gas} \left(\frac{2\pi k_B T}{m_{gas}}\right)^{1/2} \left(1 + \frac{\pi \alpha}{8}\right)$$
 (Equ. 24)

where  $\rho_{gas}$  is the mass density and  $m_{gas}$  the molecular mass of the plasma gas. Based upon this, the average diffusion velocity of particles during a particular time increment can be calculated.

#### 5 Results and Discussion

## 5.1 Flow fields

**Fig. 5** shows three flow filaments for the spray distances of 400 mm and 1000 mm each. They were calculated applying the PS-PVD flow model described in the previous section 4 starting at the top of the boundary layer at three different radial offsets from the jet axis. The thickness of the boundary layer for the 400 mm case and the 1000 mm case is similar (6.8 mm) since the effect of the temperature induced higher kinematic viscosity is compensated by the higher flow strength. Along these stream lines, the time histories of the temperatures can be determined and introduced into the nucleation and growth calculations described in section 3.4. Based on these results, the locations on the streamlines, where nucleation of particles is initiated, can be identified. They are indicated in **Fig. 5**.

Along these streamlines, the thermophoretic velocities were calculated as described in section 4.2. On the streamline #1 at 400 mm spray distance, which represents the smallest flow velocities, the

thermophoretic velocities reached 32 m s<sup>-1</sup> on average and 43 m s<sup>-1</sup> at most. This is one magnitude smaller than the gas flow velocities. For the other streamlines, this disproportion is even more pronounced. Consequently, thermophoresis was not considered in this work.

Particle displacements by diffusion were calculated according to section 4.3 for the time intervals  $\Delta t$  from the start of nucleation to the end of simulation at r = 60 mm. Plasma temperatures and particle diameters were averaged along this stream line sections. For all investigated streamlines and both spray distances, the largest diffusion velocity was found to be 82 m s<sup>-1</sup>. This is considerably smaller again than the gas flow velocities. Hence, diffusion was not considered in this work.

To check the applicability of the steady-state nucleation approach, the time constants  $\tau^*$  were determined according section 3.1. Comparing the nucleation rates for all investigated stream lines, the maximum values were found between 0.7 and  $1.3\cdot10^{23}$  m<sup>-3</sup> s<sup>-1</sup>. For the streamline #1 at 400 mm spray distance, the average nucleation time constant  $\tau^*$  was found to be  $5.8\cdot10^{-6}$  s. The time spans from nucleation onset to the end of simulation at r = 60 mm was between  $3.2\cdot10^{-4}$  s and  $2.1\cdot10^{-5}$  s. Thus, steady state nucleation prevails.

In **Fig. 6**, the time histories of the flow velocities and temperatures along the investigated stream lines through the boundary layer are given. The velocities are larger along the streamlines being located more outside since the flow spreads in radial direction and gets less close to the substrate. While **Fig. 5** shows where the onset points are located, in **Fig. 6** it can be seen when it happens. These points of time are a result of flow velocity (i.e. time for flow) and thermal history meanwhile. The onset of nucleation is initiated by reaching a sufficient nearness to the relative cold substrate. The distance to the jet axis is

less decisive. The cooling rates through the boundary layer reach 10<sup>7</sup> to 10<sup>8</sup> K s<sup>-1</sup> which is at the upper limit of what is obtained in common particle synthesis and coating deposition processes by thermal plasmas [56]. At the longer spray distance of 1000 mm, the onset of particle growth is closer to the jet axis than in the case of 400 mm, although the flow velocities are slightly higher. The reason is the dominating effect of the lower temperature so that the amount of supersaturation required for nucleation and condensation is reached earlier. This tendency means that at 400 mm, the coating deposition in the central part of the jet profile can be expected to occur mainly directly from vapor phase via heterogeneous nucleation while at 1000 mm, the zone with homogeneous nucleation and particle formation would move closer to the jet axis.

### 5.2 Particle formation

**Fig. 7** gives the developments in time of the vapor molecule concentration  $n_I$ , the particle concentration per unit volume  $n_g$ , and the total particle volume per unit volume  $n_g \cdot v_g$  for the stream lines #1 at 400 mm and 1000 mm spray distance in **Fig. 5**, respectively. In both cases, nucleation starts at a temperature of approx. 2600 K. At the longer spray distance, nucleation starts earlier due to the lower temperature level.

The gradients of the nucleation developments indicate that the nucleation rates decrease again after reaching a maximum, **Fig. 8**; this occurs when temperatures drop below approx. 1800 K to 1900 K. The retardation of nucleation is mainly a consequence of the steadily increasing supersaturation ratio S and how it affects the different constituent factors of the nucleation rate J, see Equ. 4. On the other hand, particles grow increasingly by condensation. Generally more particles are generated at the shorter spray distance since more time is available.

At both spray distances, coagulation becomes relevant when enough particles are generated and reach a concentration  $n_g$  of approx.  $10^{19}$  m<sup>-3</sup>. The particle collision frequencies  $\beta_{gg}$  (Equ. 9) are of the same magnitude in both cases. The characteristic times for coagulation  $\tau_{coal}$  are found to be almost always substantially shorter for both liquid (Equ. 10) and solid particles (Equ. 11) than the collision times  $\tau_{coll}$  (Equ. 13). Only in the very last sections of streamlines #1 and #2 at 1000 mm, the coagulation time for solid particles exceeds the collision times due to the low temperatures. However, the formation of some irregular shaped solid aggregates is unlikely. Fujita found that the transition between fast-diffusion liquid-like and slow-diffusion crystalline properties takes place abruptly with size of the clusters, which he referred to as a magic size. He determined the magic size for an embedded ZrO<sub>2</sub> cluster to be approx. 6 nm at room temperature [57]. The magic size for the isolated state was expected to be approx. 12 nm [58]. Moreover, because of their very small size, the droplets in principle solidify at significantly lower temperature than the bulk melting point of the solid [40]. This allows the assumption that fast coalescence of two particles after their collision [44] yielding rather spherical shaped secondary particles.

In **Fig. 9**, the average particle diameters  $< d_p >$  obtained by the monodisperse approach (cf. section 3.4) are given for the two flow filaments #1 in **Fig. 5**. They are obtained by dividing the total volume of particles  $v_g$  divided by their number  $n_g$ . Thus, they are averages by particle number. To know more about the effect on the coating microstructure, a volumetric average would be more expressive. However, this cannot be obtained from the applied simple monodisperse approach.

The plots of the average particle size in **Fig. 9** start at the onset of particle nucleation. Initially, particle diameters of approx. 4.5 nm (corresponds to approx. 1500 molecules) are obtained as the critical particle

size is still larger at higher temperatures. After decreasing below 1 nm, a slow increase follows again. This is because on the one hand, existing particles begin to grow by condensation; on the other hand, new particles with a small critical size nucleate. At the end of the modelling domain where at high supersaturation the critical nuclei size  $g^*$  approaches molecular dimensions, average particle diameters reach approx. 0.5 nm. This corresponds to cluster sizes of 2-3 molecules. Thus, the application limits of the homogeneous nucleation approach mentioned in section 3.1 are reached.

As the particles are very small, they will closely follow the plasma flow . This can be expressed by the dimensionless Stokes number quantifying the significance of the particle inertia if the flow direction of the fluid changes. Under the conditions investigated here, Stokes numbers are expected to be significantly below unity which is the critical criterion to detach from the flow.

# 5.3 Particle flux

The local particle volume fluxes per unit area were calculated as products of the total particle volume density per unit gas volume  $v_g$  and the gas flow velocity v. They can be interpreted as coating deposition rates assuming that all the particles are deposited and form an ideally dense coating. **Fig. 10** gives such coating deposition rates determined along the streamlines #1, 2, and 3 in **Fig. 5** at 400 mm and 1000 mm spray distance, respectively. Considerable deposition rates are obtained only in the edge regions of the plasma jet. It should be noted that only the deposition of particles homogeneously nucleated and grown in-flight was studied in this work but no heterogeneous nucleation on the substrate. At the short spray distance of 400 mm, no significant particle deposition is obtained in the center region of jet at  $r \le 40$  mm.

In spray experiments [59], the following deposition rates were observed at r = 40 mm: 32  $\mu\text{m min}^{-1}$  (400 mm) and 24  $\mu\text{m min}^{-1}$  (1000 mm). The comparison with the calculated data shows that in the outer regions of the jet, the deposition can result partially from particles while in the center region direct condensation from the vapor phase on the substrate surface must be assumed to prevail. At 1000 mm spray distance, the particle deposition generally increases and occurs also closer to the jet axis. It is noteworthy that the calculated flux of condensed clusters is found to be approx. tenfold if the powder feed rate is increased by a factor of nearly 3 from 7 to 20 g min $^{-1}$ .

# 6 Summary and Conclusion

This work was initiated by considerations on the importance of the boundary layer for the deposition of nano-sized structures from literature as well as by previous own experimental results from PS-PVD. A boundary layer kinetics model was coupled to a model for homogeneous nucleation and particle growth by condensation and coagulation. The analytical models for the boundary layer kinetics and particle formation and growth proved to be worthwhile as they were able to resolve the steep gradients of the boundary layer properties. Calculations were carried out for zirconia deposition through an axisymmetric plasma gas flow onto a plane substrate under typical PS-PVD conditions. Two spray distances 400 mm and 1000 mm (standard) and different radial offsets from jet axis up to 60 mm were considered.

The main results are as follows:

- Homogeneous nucleation and growth of nano-sized particles is possible in the boundary layer of substrates under PS-PVD conditions.
- Sufficiently low temperature (and thus high supersaturation) is the main criterion for the onset of particle nucleation and growth.

- At short spray distance, the onset of particle nucleation and growth occurs in distinct radial
  offset from the jet axis while at long standard spray distance the onset moves closer to the
  plasma jet center.
- The flux of condensed particles increases at longer spray distance and radial distance to the jet axis; its contribution to the total coating growth can reach more than 10%.
- Increasing the powder feed rate from 7 to 20 g min<sup>-1</sup> the flux of condensed clusters is approx. tenfold.
- The particle size is very small in the range of single nanometers. Microstructures or crystallographic orientations are unlikely to be affected by this cluster deposition.

### References

- 1. von Niessen K, Gindrat M (2011) Plasma Spray-PVD: A New Thermal Spray Process to Deposit Out of the Vapor Phase. J Therm Spray Technol 20: 736-743
- 2. Mauer G (2014) Plasma Characteristics and Plasma-Feedstock Interaction Under PS-PVD Process Conditions, Plasma Chem. Plasma Proc. 34(5): 1171-1186
- 3. von Niessen K, Gindrat M, Refke A (2010) Vapor Phase Deposition Using Plasma Spray-PVD. J Therm Spray Technol 19: 502-509
- 4. Hospach A, Mauer G, Vaßen R, Stöver D (2012) Characteristics of Ceramic Coatings Made by Thin Film Low Pressure Plasma Spraying (LPPS-TF). J Therm Spray Technol 21: 435–440
- 5. Mauer G, Hospach A, Vaßen R (2013) Process development and coating characteristics of plasma spray-PVD. Surf Coat Technol 220: 219–224
- 6. Rezanka S, Mauer G, Vaßen R (2014) Improved Thermal Cycling Durability of Thermal Barrier Coatings Manufactured by PS-PVD. J Therm Spray Technol 23: 182-189
- 7. Rezanka S (2015) Abscheidung von Wärmedämmschichtsystemen mit dem Plasma Spray-Physical Vapor Deposition- (PS-PVD) Prozess Untersuchung des Prozesses und der hergestellten Schichten (in German). PhD thesis, Ruhr Universität Bochum, Schriften des Forschungszentrums Jülich, Reihe Energie & Umwelt Vol. 290
- 8. Mauer G, Hospach A, Zotov N, Vaßen R (2013) Process Conditions and Microstructures of Ceramic Coatings by Gas Phase Deposition Based on Plasma Spraying, J. Therm. Spray Technol. 22(2-3): 83-89
- 9. Li C, Guo H, Gao L, Wei L, Gong S, Xu H (2015) Microstructures of Yttria-Stabilized Zirconia Coatings by Plasma Spray-Physical Vapor Deposition. J. Therm. Spray Technol. 24(3): 534-541

- Hafiz J, Mukherjee R, Wang X, McMurry PH, Heberlein JVR, Girshick SL (1996) Hypersonic Plasma Particle Deposition - A Hybrid between Plasma Spraying and Vapor Deposition. J Therm Spray Technol 15(4): 822-826
- 11. Beaber AR, Hafiz J, Heberlein JVR, Gerberich WW, Girshick SL (2008) Wear behavior in SiC-TiX multilayered nanocomposite coatings. Surf Coat Technol 203: 771-775
- 12. Girshick SL, Chiu C-P, Muno R, Wu CY, Yang L, Singh SK, McMurry PH (1993) Thermal plasma synthesis of ultrafine iron powders. J Aerosol Sci 24(3): 367-382
- 13. Bilodeau J-F, Proulx P (1996) A Mathematical Model for Ultrafine Iron Powder Growth in a Thermal Plasma. Aerosol Sci Technol 24(3): 175-189
- 14. Rao N, Girshick S, Heberlein J, McMurry P, Jones S, Hansen D, Micheel B (1995) Nanoparticle Formation Using a Plasma Expansion Process. Plasma Chem Plasma Proc 15(4): 581-606
- 15. Yoshida T (1990) The Future of Thermal Plasma Processing. Mater Trans, JIM 31(1): 1-11
- 16. Yoshida T (1994) The future of thermal plasma processing for coating. Pure Appl Chem 66(6): 1223-1230
- 17. Yoshida T (2006) Toward a new era of plasma processing. Pure Appl Chem 78(6): 1093-1107
- 18. Shigeta M, Murphy AB (2011) Thermal plasmas for nanofabrication. J Phys D: Appl Phys 44: 174025 (16pp)
- 19. Terashima K, Yamaguchi N, Hattori T, Takamura Y, Yoshida T (1998) High rate deposition of thick epitaxial films by thermal plasma flash evaporation. Pure Appl Chem 70(6): 1193-1197
- 20. Kambara M, Hamai Y, Yagi H, Yoshida T (2007) Nano cluster assisted high rate epitaxy of silicon by mesoplasma CVD. Surf Coat Technol 201: 5529-5532
- 21. Han P, Yoshida T (2002) Growth and transport of clusters in thermal plasma vapor deposition of silicon. J Appl Phys 92(8): 4772-4778
- 22. Han P, Yoshida T (2002) Numerical investigation of thermophoretic effects on cluster transport during thermal plasma deposition process. J Appl Phys 91(4): 1814-1818
- 23. Bouyer E, Henne RH, Müller M, Schiller G (2001)  $Si_3N_4$  Fibers Synthesized by Thermal Plasma CVD. Chem Vap Deposition 7(4): 139-142
- 24. Tashiro S, Zeniya T, Yamamoto K, Tanaka M, Nakata K, Murphy AB, Yamamoto E, Yamazaki K, Suzuki K (2010) Numerical analysis of fume formation mechanism in arc welding. J. Phys. D: Appl. Phys. 43: 434012 (12pp)
- 25. Tashiro S, Murphy AB, Matsui S, Tanaka M (2013) Numerical analysis of the influence of particle charging on the fume formation process in arc welding. J. Phys. D: Appl. Phys. 46: 224007 (9pp)
- 26. Hospach A (2012) Untersuchungen zum Thin FilmLow Pressure Plasma Spraying (LPPS-TF) Prozess (in German). PhD thesis, Ruhr Universität Bochum, Schriften des Forschungszentrums Jülich, Reihe Energie & Umwelt Vol. 140
- 27. Mauer G, Vaßen R (2012) Plasma Spray-PVD: Plasma Characterization and Impact on Coating Properties. J. Phys.: Conf. Ser. 406: 012005
- 28. Rösner-Kuhn M, Hofmeister WH, Kuppermann G, Bayuzick RJ, Frohberg MG (1999) Investigations of the influence of oxygen on the surface tension of zirconium by the oscillating drop technique. Surf Sci 443(3): 159–164
- 29. Moradian A, Mostaghimi J (2005) High Temperature Surface Tension Measurement. IEEE Trans Plasma Sci 33(2): 410-411

- 30. Shinoda K, Kojima Y, Yoshida T (2005) In Situ Measurement System for Deformation and Solidification Phenomena of Yttria-Stabilized Zirconia Droplets Impinging on Quartz Glass Substrate under Plasma-Spraying Conditions. J Therm Spray Technol 14(4): 511-517
- 31. Gordon S, McBride BJ (1994) Computer Program for Calculation of Complex Chemical Equilibrium Compositions and Applications Analysis. NASA-Reference Publication, 1311 part 1
- 32. Gordon S, McBride BJ (1996) Computer Program for Calculation of Complex Chemical Equilibrium Compositions and Applications User's Manual and Program Description. NASA-Reference Publication 1311, part 2
- 33. Knacke O (1991) Thermochemical properties of inorganic substances, 2<sup>nd</sup> ed., Springer, Berlin
- 34. Samsonov GV, Ed. (1986) The Oxide Handbook. 2nd ed., IFI/Plenum, New York, NY
- 35. Girshick SL, Chiu C-P (1990) Numerical study of MgO powder synthesis by thermal plasma. J Aerosol Sci 21(5): 641-650
- 36. Girshick SL (1994) Particle nucleation and growth in thermal plasmas. Plasma Sources Sci Technol 3(3):388-394
- 37. W Thomson (Lord Kelvin) (1871) On the equilibrium of vapour at a curved surface of liquid. Philos Mag (1798-1977) 42(282): 448-452
- 38. Katz JL, Wiedersich H (1977) Nucleation theory without Maxwell Demons. J Colloid Interface Sci 61(2): 351-355
- 39. Girshick SL, Chiu C-P (1990) Kinetic nucleation theory: A new expression for the rate of homogeneous nucleation from an ideal supersaturated vapor. J Chem Phys 93(2): 1273-1277
- 40. Friedlander SK (2000) Smoke, dust, and haze: Fundamentals of aerosol dynamics. 2<sup>nd</sup> ed, Univ. Press, Oxford UK
- 41. Flagan RC, Seinfeld JH (2012) Fundamentals of Air Pollution Engineering. Dover Publications Inc. Mineola, NY
- 42. Abraham FF (1974) Hogogeneous Nucleation Theory. Academic Press, New York/London
- 43. Feder J, Russel KC, Lothe J, Pound GM (1966) Homogeneous nucleation and growth of droplets in vapours. Adv Phys 15: 111-178
- 44. Vorobev A, Zikanov O, Mohanty P (2008) Modelling of the in-flight synthesis of TaC nanoparticles from liquid precursor in thermal plasma jet. J Phys D: Appl Phys 41: 085302 (15pp)
- 45. Frenkel J (1945) Viscous flow of crystalline bodies under the action of surface tension. J Phys (USSR) 9(5): 385-391
- 46. Friedlander SH, Wu MK (1994) Linear rate law for the decay of the excess surface area of a coalescing solid particle. Phys Rev B: Condens Matter Mater Phys 49(5):3622-3624
- 47. Cipitria A (2008) Sintering of Plasma-Sprayed Thermal Barrier Coatings. PhD thesis, University of Cambridge, in: Cipitria A, Golosnoy IO, Clyne TW (2009) A sintering model for plasma-sprayed zirconia TBCs. Part I: Free-standing coatings. Acta Mater 57: 980–992
- 48. Hawa T, Zachariah MR (2006) Coalescence kinetics of unequal sized nanoparticles. J Aerosol Sci 37(1): 1-15
- 49. Nemchinsky VA, Shigeta M (2012) Simple equations to describe aerosol growth. Modelling Simul Mater Sci Eng 20: 045017 (11pp)
- v. Smoluchowski, M (1916) Drei Vorträge über Diffusion, Brownsche Molekularbewegung und Koagulation von Kolloidteilchen (part 3, in German). Phys Z 17 (1916): 585-599

- 51. Homann F (1936) Der Einfluß großer Zähigkeit bei der Strömung um den Zylinder und um die Kugel (in German). Z Angew Math Mech 16(3): 153-164
- 52. Frössling N (1940) Evaporation, heat transfer, and velocity distribution in two-dimensional and rotationally symmetrical laminar boundary-layer flow(translation) NACA technical memorandum 1432, Washington, 1958
- 53. Pohlhausen E (1921) Der Wärmeaustausch zwischen festen Körpern und Flüssigkeiten mit kleiner Reibung und kleiner Wärmeleitung (in German). Z Angew Math Mech 1(2): 115–121
- 54. Chen X, Pfender E (1983) Effect of the Knudsen Number on Heat Transfer to a Particle Immersed into a Thermal Plasma. Plasma Chem. Plasma Proc. 3(1): 97-113
- 55. Einstein A (1905) Über die von der molekularkinetischen Theorie der Wärme geforderte Bewegung von in ruhenden Flüssigkeiten suspendierten Teilchen (in German). Ann Phys 322(8): 549-560
- 56. Fauchaus P, Vardelle A, Denoirjean A (1997) Reactive thermal plasmas: ultrafine particle synthesis and coating deposition. Surf Coat Technol 97: 66–78
- 57. Fujita H (1991), Atom Clusters New Applications of High-Voltage Electron Microscopy "Micro-Laboratory" to Materials Science, Ultramicroscopy 39(1-4):, 369-381
- 58. Jeon I-D, Gueroudji L, Kim D-Y, Hwang N-M (2001) Temperature Dependence of the Deposition Behavior of Yttria-stabilized Zirconia CVD Films: Approach by Charged Cluster Model. J Korean Ceram Soc, 38(3): 218-224
- 59. He W (2017) Deposition Mechanisms of Thermal Barrier Coatings (TBCs) Manufactured by Plasma Spray-Physical Vapor Deposition (PS-PVD). PhD thesis, Ruhr Universität Bochum, Schriften des Forschungszentrums Jülich, Reihe Energie & Umwelt Vol. 398

# **Tables**

**Table 1** Plasma jet temperatures and velocities at two investigated spray parameters

Spray distance	400 mm	1000 mm
Plasma gas temperature $T_{\infty}$	4120 K	4275 K
Plasma gas velocity $v_{z,\infty}$	-1400 m s <sup>-1</sup>	-1200 m s <sup>-1</sup>
Substrate temperature $T_{sub}$	2270 K	1250 K

Table 2 Boundary layer data

Spray distance	400 mm	1000 mm
Integral temperature	3270 K	3050 K
Average kinematic viscosity v	0.864 m <sup>2</sup> s <sup>-1</sup>	0.762 m <sup>2</sup> s <sup>-1</sup>
Flow strength <i>a</i>	1.45 10 <sup>5</sup> s <sup>-1</sup>	1.30 10 <sup>5</sup> s <sup>-1</sup>
Boundary layer thickness $\delta_v$	6.8 mm	6.8 mm

# **Figures**

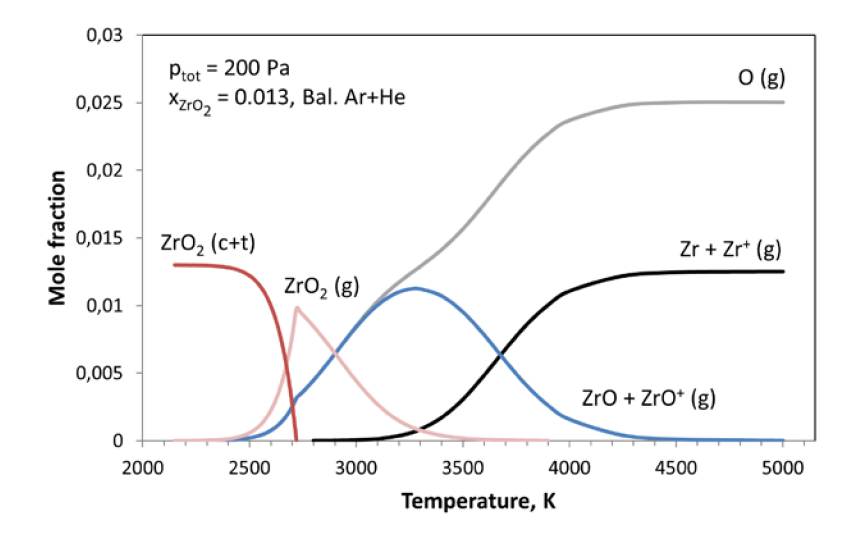


**Fig. 1** Calculated chemical equilibria of ZrO<sub>2</sub>, ZrO, Zr, O<sub>2</sub>, and O in the Ar-He plasma gas mixture; the subscript (c+t) denotes the sum of solid crystalline cubic and tetragonal phases, the subscript (g) denotes gaseous phases.

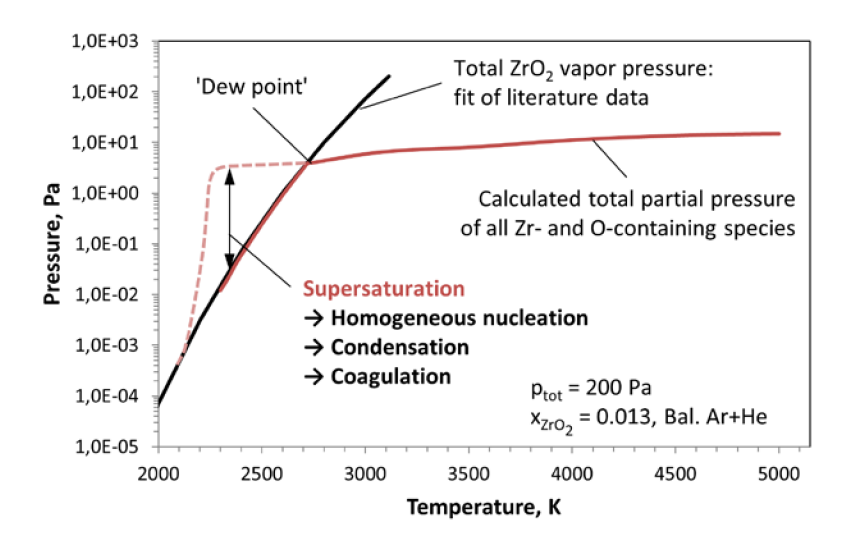


Fig. 2 Total vapor pressure data of  $ZrO_2$  according to a fit [7] of literature data (Equ. 1); the total partial pressure of all gaseous species generated by the evaporation of zirconia was superimposed; the dotted curve schematically indicates the development of supersaturation during fast cooling.

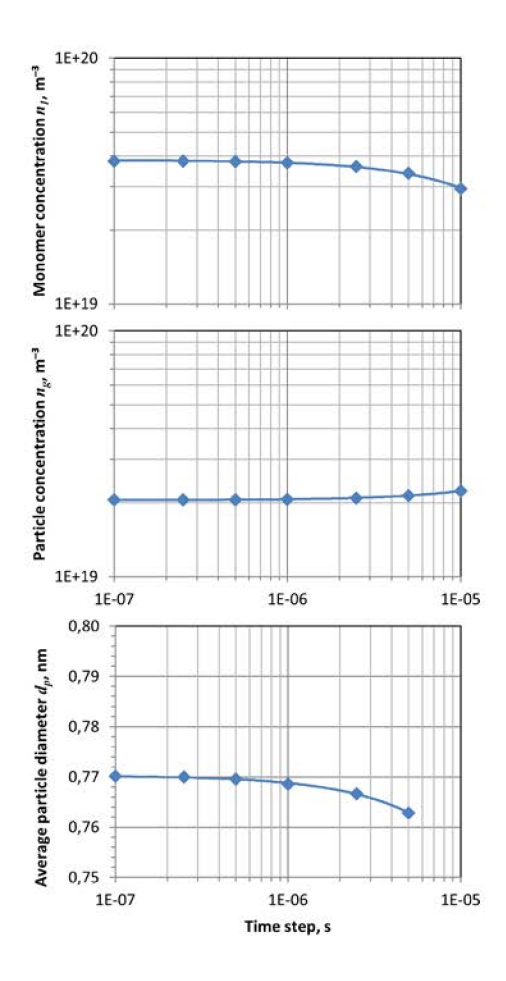


Fig. 3 Final monomer number density  $n_1$ , particle number density  $n_g$ , and average particle diameter  $< d_p >$  calculated for  $t = 10^{-4}$  s and plotted against the time step width  $\Delta t$  applied for integration.

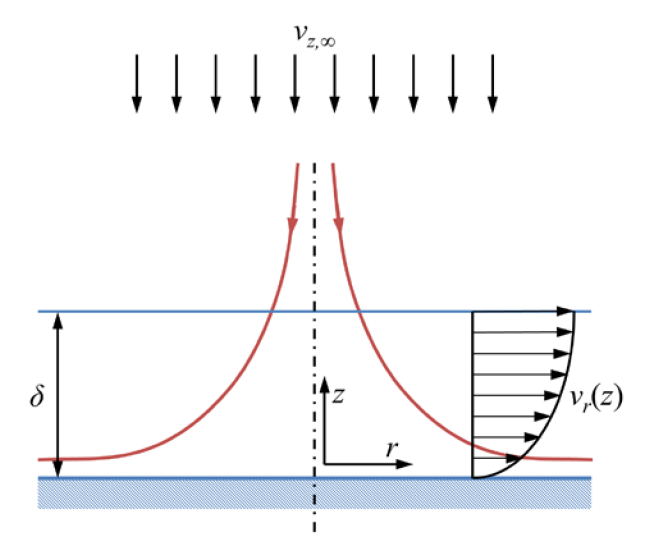
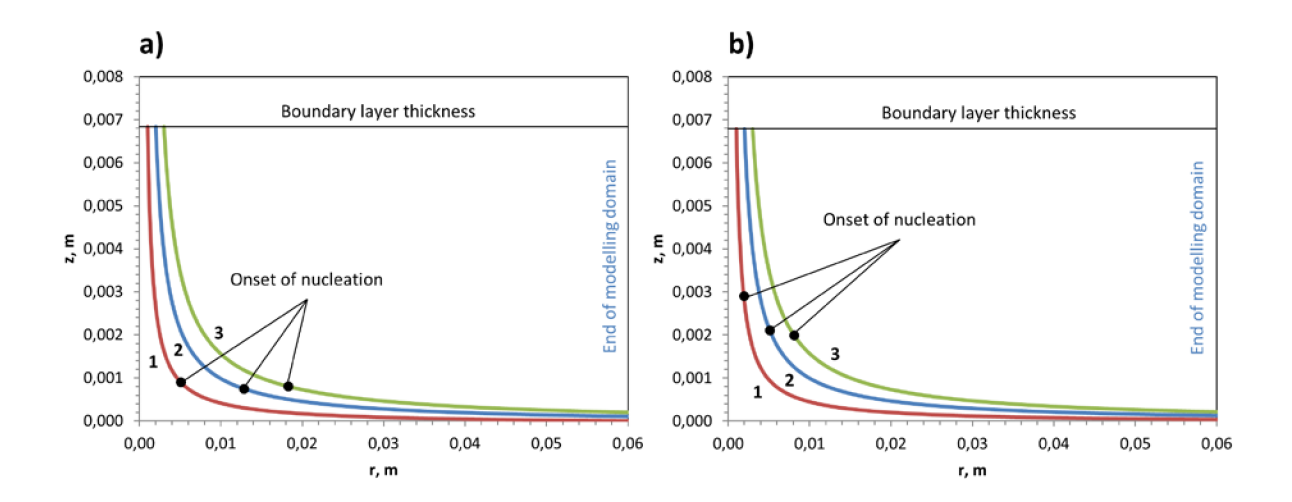
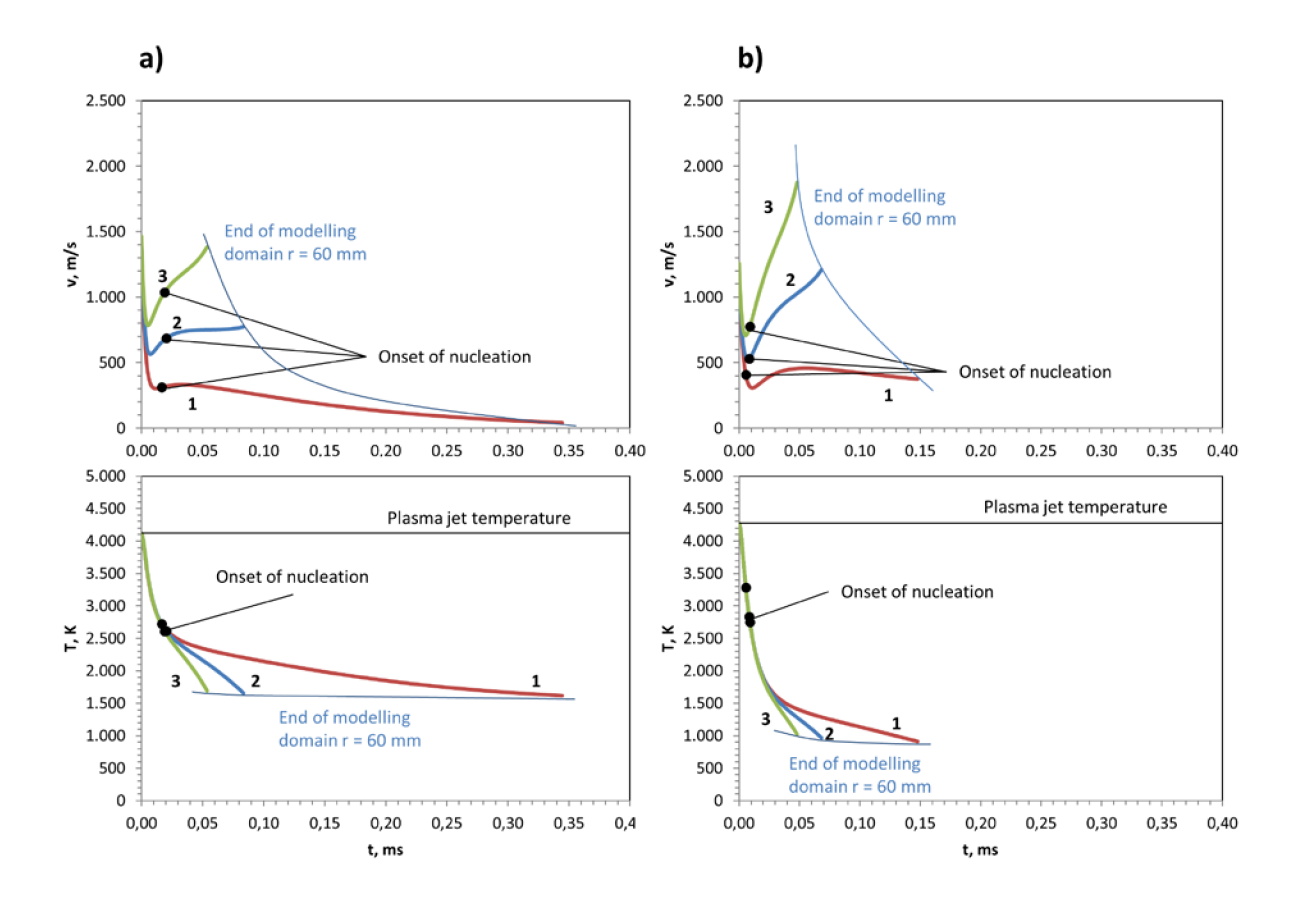


Fig. 4 Model of an axisymmetric (plasma) flow normal to a plate (substrate); schematic representation.



**Fig. 5** Three stream lines of the plasma gas without particles, each calculated for the spray distances of a) 400 mm and b) 1000 mm; r = 0 mm refers to the jet axis. Note that r and the z axes have different scales.



**Fig. 6** Time history of the plasma gas velocities (top) and temperatures (bottom) along the flow filaments through the boundary layer, each calculated for the spray distances of a) 400 mm and b) 1000 mm.

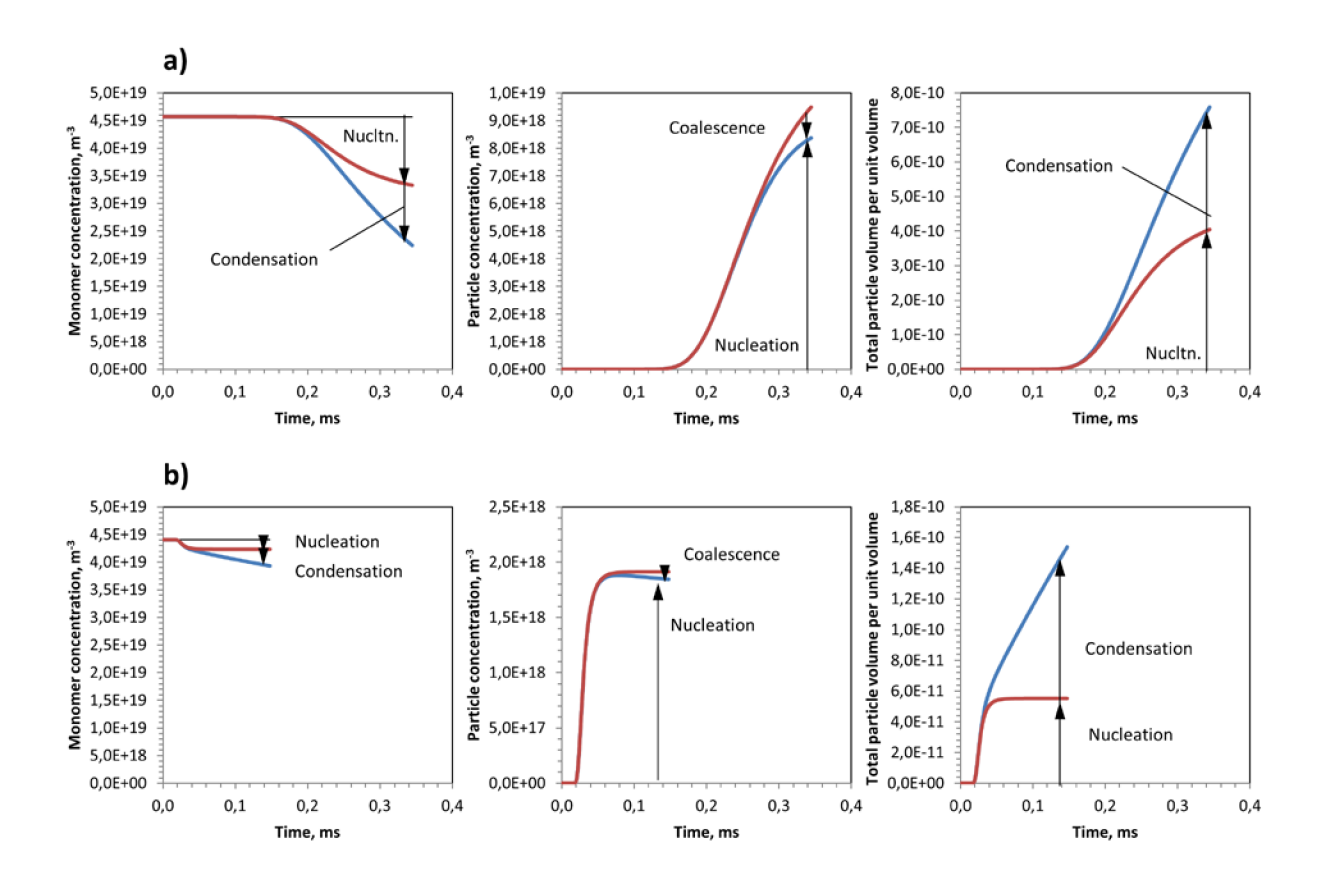
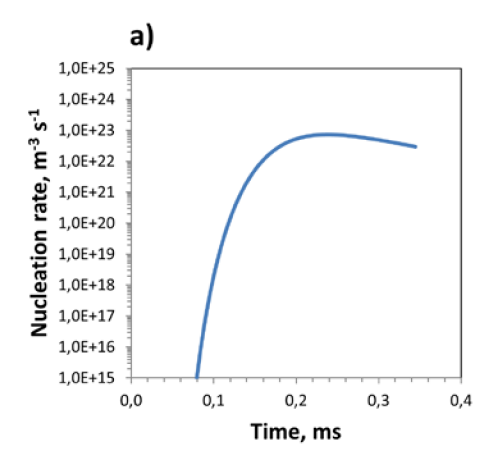
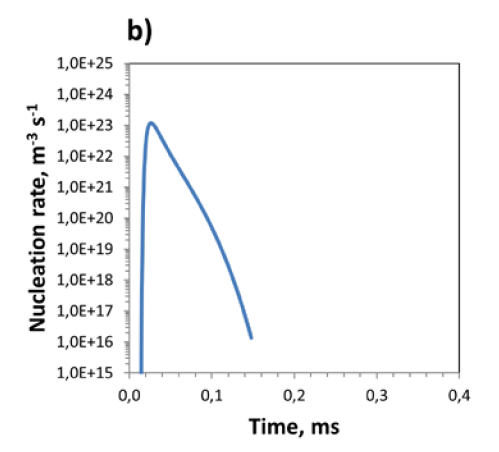
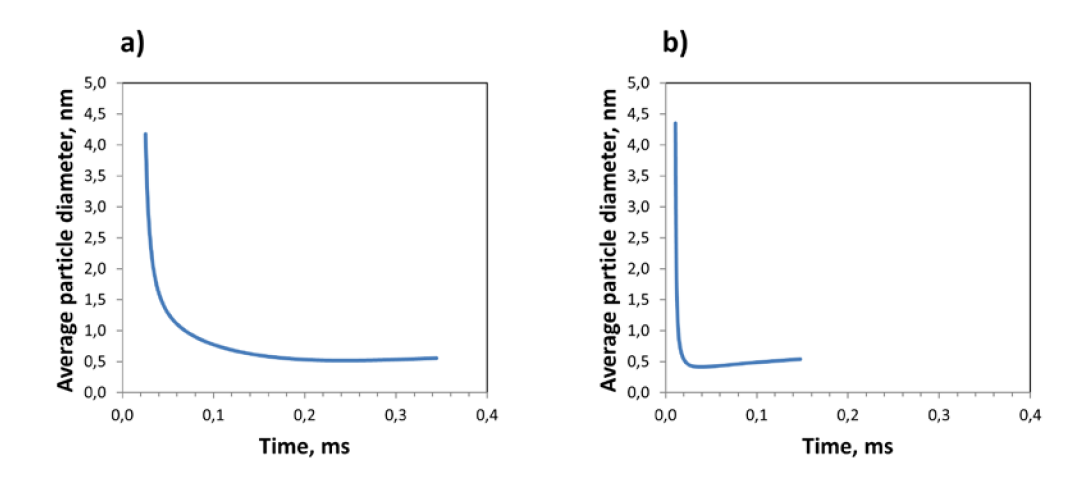


Fig. 7 Developments in time of the vapor molecule concentration  $n_1$ , the particle concentration per unit volume  $n_g$ , and the total particle volume per unit volume  $n_g \cdot v_g$  for the stream lines #1 in Fig. 5 at a) 400 mm and b) 1000 mm spray distance, respectively.





**Fig. 8** Nucleation rates for the two stream lines #1 in **Fig. 5** at a) 400 mm and b) 1000 mm spray distance, respectively; the plots start at the onset of particle nucleation.



**Fig. 9** Average particle diameters  $< d_p >$  for the two stream lines #1 in **Fig. 5** at a) 400 mm and b) 1000 mm spray distance, respectively; the plots start at the onset of particle nucleation.

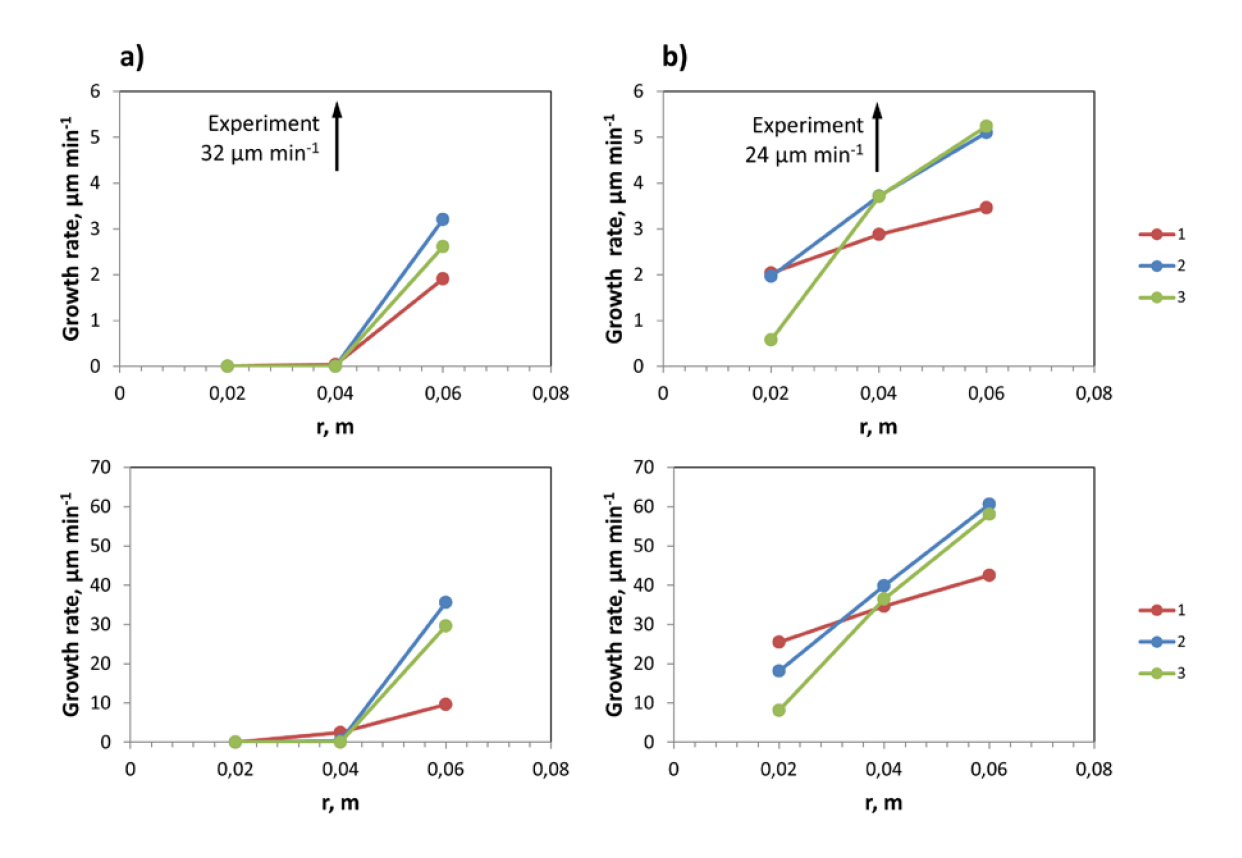


**Fig. 10** Growth rates determined from particle volume fluxes along the streamlines #1, 2, and 3 in **Fig. 5** for powder feed rates of 7 g min<sup>-1</sup> (top) and 20 g min<sup>-1</sup> (bottom) at a) 400 mm and b) 1000 mm spray distance, respectively.